

A filter inspired by deep-sea glass sponges for oil cleanup under turbulent flow

Received: 20 June 2024

Accepted: 11 December 2024

Published online: 02 January 2025

 Check for updatesYuan Yu¹, Chi Ding², Jinna Zhang¹, Nanqi Ren¹, Chuyang Y. Tang^{3,4} & Shijie You¹✉

Oil spill disasters lead to widespread and long-lasting social, economical, environmental and ecological impacts. Technical challenges remain for conventional static adsorption due to hydrodynamic instability under complex water-flow conditions, which results in low oil-capture efficiency, time delay and oil escape. To address this issue, we design a vortex-anchored filter inspired by the anatomy of deep-sea glass sponges (*E. aspergillum*) by mimicking their exceptional skeletal features and filter-feeding patterns. Results demonstrate that the vortex-anchored filter can retain external turbulent-flow kinetic energy in low-speed vortical flow with small Kolmogorov microscale (85 μm) in the cavity of skeleton, leading to enhanced interfacial mass transfer and residence time by physical field synergy. It improves hydrodynamic stability by reducing Reynolds stresses in nearly quiescent wake flow. The vortex-anchored filter can realize >97% capture of floating, underwater and emulsified oils stably at Reynolds numbers ranging from subcritical to supercritical regimes. This study not only highlights the importance of vortex-anchored mechanism in enhancing interfacial mass transfer and hydrodynamic stability during oil capture beyond previously known benefits of increased residence time, but also represents a paradigm shift to advance biophysically inspired strategies for in-situ, dynamic and robust cleanup of spilled oil, environmental remediation and resource recovery.

Oil spill disasters may occur anywhere the oil is drilled, processed, stored and transported^{1–3}. Oil spills can contaminate surrounding waters thousands of times their volume, resulting in widespread and long-lasting social, economic, environmental and ecological impacts^{1–3}. It is common practice to use oleophilic adsorbent materials for in-situ capture of spilled oil. For example, in the accidents of the 2010 Deepwater Horizon and the 2023 MT Princess Empress, spilled oil was collected by using adsorbent booms modified by oleophilic polymers such as polysiloxanes, organosilanes, polypropylene and polyurethane^{4,5}. To expand the oil-solid interface, functionalized trawl nets⁶, separator-skimmers⁷ and floating wells⁸

are applied under static mode. However, a common challenge faced by these technologies is their sensitivity to water-flow fluctuation. This will lead to severe performance loss in terms of mechanical robustness, interfacial mass transfer and oil capture efficiency, as a consequence of inhomogeneous, unstable and uncontrollable hydrodynamic behaviors of oil-capture matrixes. Such issues are commonly encountered for oil-in-water emulsion in the case of pipeline leakage and offshore industrial discharge. Therefore, there is a strong incentive to develop effective solutions for dynamic robust cleanup of spilled oil under complex hydrodynamic conditions.

¹State Key Laboratory of Urban Water Resource and Environment, School of Environment, Harbin Institute of Technology, Harbin 150090, P. R. China. ²Beijing Engineering Corporation Limited, Power China, Beijing 100024, P. R. China. ³Department of Civil Engineering, The University of Hong Kong, Hong Kong, SAR 999077, P. R. China. ⁴Materials Innovation Institute for Life Sciences and Energy (MILES), HKU-SIRI, Shenzhen 518000, P.R. China. ✉e-mail: sjyou@hit.edu.cn

Nature may offer inspiring solutions. A large number of previous studies reported bio-inspired strategies for oil-water separation. For example, cobwebs⁹, marine mussels¹⁰, cat-tongues¹¹, and nepenthes-peristomes¹² provided inspirations for designing superhydrophobic materials and interfaces. Manta rays inspired the nanofiberous membrane for oil-water separation by non-clogging ricochet filtration^{13,14}, and filter-feeding fish inspired the helical, cross-step filter for collecting harmful algae¹⁵. However, these works mainly focused on modifying interfacial properties and mass transfer modes for oil-adsorbing materials (e. g. hydrophobicity/hydrophilicity and oleophobicity/oleophilicity), but their hydrodynamic stability remains unclear. Low hydrodynamic robustness would result in low oil-capturing efficiency, time delay and oil escape, especially under turbulent flow.

In nature, deep-sea glass sponge (e. g. *E. aspergillum* or Venus' flower basket)^{16–18} attracts our interest because its exceptional structures are closely connected with what we are searching for with respect to spilled oil capture. Unlike shallow-water sponges that benefit from nutritious photosynthetic algae, feeding of deep-sea sponges is quite challenging in the deep sea with complex flow, scarce nutrients and shallow anchorage. *E. aspergillum* can achieve filter feeding with high effectiveness, high selectivity and high robustness, originating from its mechanical architecture¹⁶. Specifically, *E. aspergillum* has the multi-layered skeleton-flagellum architecture as illustrated schematically in Fig. 1a and Supplementary Fig. 1^{19,20}. As water stream flows through the sponge body of *E. aspergillum*, the multi-angle struts create 3D streamlines with frequent collision, deflection, convergence and separation. Then, the macro-scale turbulent flow is dissipated,

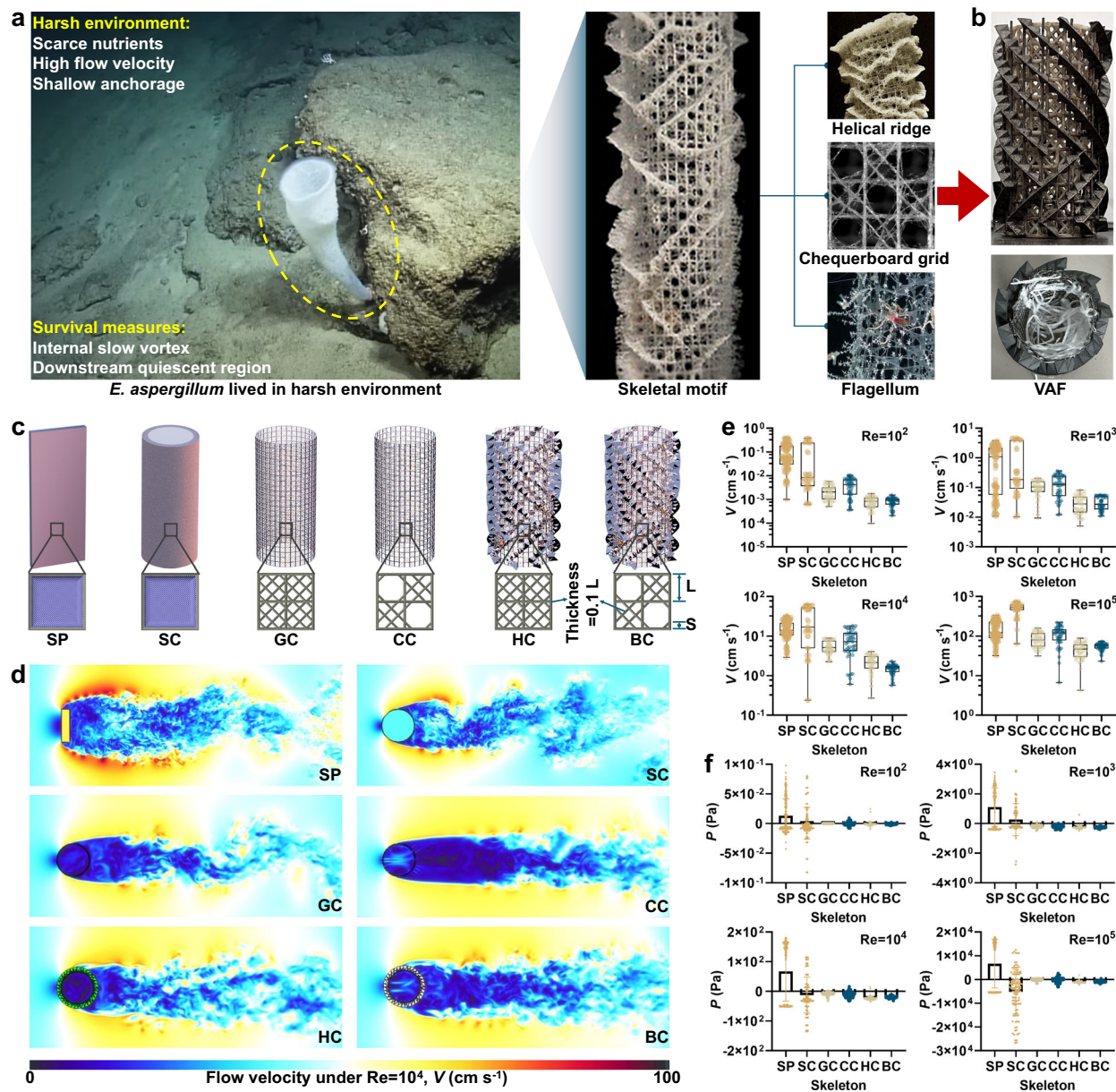


Fig. 1 | Bio-inspired design for vortex-anchored filter (VAF). **a** Skeletal motifs of deep-sea *E. aspergillum*, whose food particles shared similarity with oil droplets^{16,47}. **b** Front and top views of bio-inspired VAF with bio-inspired hollow cylinder (BC) skeleton and flagellum-adsorbent. **c** Models of oil-capture matrixes for different skeletons, including solid plate (SP), solid cylinder (SC), grid hollow cylinder (GC), chequerboard hollow cylinder (CC), helical ridge-grid hollow cylinder (HC), and BC

(more details in Supplementary Text 2). **d–f** Impact of skeletal motifs on **(d)** the flow pattern at supercritical regime, **(e)** the magnitude of flow velocity and **(f)** the pressure at discrete nodes in adsorption region under different Re numbers. Note: The thickness is 0.1 L for horizontal, vertical, and diagonal elements in the grids of GC, CC, HC, and BC. Source data are provided as a Source Data file.

resulting in small-scale low-speed vortical flow within the body cavity over subcritical and critical regimes ($Re < 5 \times 10^3$)¹⁷. The swirling flow patterns hold the key to reducing hydrodynamic load, capturing nutrients by flagellum and maintaining mechanical stability. This allows the *E. aspergillum* to thrive via aeons of natural selection at depths ranging from 100 to 1000 meters in the Pacific Ocean and around Antarctica¹⁸.

The anatomy of *E. aspergillum* provides an elegant biophysical inspiration for designing the skeletal architecture of oil capture filter toward high mass transfer and hydrodynamic stability. By mimicking the filter-feeding patterns of deep-sea glass sponge during oil capture, the vortex-anchored flow pattern would be expected over subcritical to supercritical regimes. Theoretically, this would realize (i) enhanced interfacial mass transfer of oil adsorption as low-speed vortical flow can promote field synergy between concentration gradient and velocity, thereby oil can be captured more effectively by increasing residence time when water-oil mixture is filtered, and (ii) increased hydrodynamic stability of the oil-capture matrix through dissipating water-flow kinetic energy and thus attenuating the drag force in nearly quiescent wake flow, which makes it highly resistant to bending stress generated by boundary-layer separation of viscous fluid. Drawing inspiration from biophysical similarities to skeletal features and filter-feeding patterns of deep-sea glass sponge, we attempted to develop a vortex-anchored filter (VAF) that may be applicable for in-situ, dynamic and robust oil cleanup under turbulent flow.

Results

Bio-inspired design for vortex-anchored filter

Inspired by the filter-feeding pattern of *E. aspergillum*, we propose the principle for designing vortex-anchored filter (VAF) by mimicking the structure of *E. aspergillum* in terms of outer skeleton and inner flagellum (Fig. 1b). The primary function of outer skeleton, made of helical ridge and chequerboard lattice, is to create slow vortex field in the cavity and quiescent regions in the wake¹⁷, so that mass transfer and hydrodynamic stability can be achieved under turbulent flow. The inner flagellum-shaped adsorbent provides a large interfacial area oil adsorption. To this end, hydrophobic melamine resin²¹ (total length of 2 cm and diameter of 0.1 cm; Supplementary Fig. 2) was embedded onto the inner wall of skeleton that was 3D-printed by stainless steel (Supplementary Fig. 3).

The helical-ridge and chequerboard-lattice structure are believed to play the central role in the VAF design. Therefore, prior to 3D printing of VAF, we performed lattice Boltzmann simulation of the structural feature of skeletal motifs in terms of grid width (L) and strut position (S/L ; Fig. 1c) to gain mechanistic insights. First, the skeleton motif was designed with the $16-L$ height and $10-L$ diameter, in which the helical ridge was designed as a diagonal ring structure consisting of semi-octahedra with L -width (Fig. 1c and Supplementary Fig. 3). Second, two optimization problems were formulated to identify the value of L and S/L that resulted in the highest flow vorticity inside cavity and lowest flow velocity in wake. The two optimization problems were solved under supercritical regime (i.e., Reynolds number of 10^5) by using Covariance Matrix Adaptation Evolution Strategy algorithm (CMA-ES)²² (Supplementary Text 1). Standard bounce-back procedure was used to deal with the coupling between fluid and solid (i.e. skeleton and flagellum). For structural optimization, we varied L and S/L one by one while keeping the other parameter constant. As shown in Fig. 1d and Supplementary Fig. 4, the skeleton motif was of extreme importance to the hydrodynamic feature. Indeed, some undesirable motifs not only impeded the generation of internal vortex, but also disrupted the stabilization of wake flow, even leading to vortex street shedding²³ (Fig. 1d). On the contrary, grid width (L) had a less significant impact on the flow pattern under each Re value (Supplementary Fig. 4), indicated by the fact that changes of L only led to a maximum change lower than 27% in vorticity. Based on above consideration, we design VAF with $L=5$

mm and $S/L=0.3$, accounting for total geometric size of 5-cm diameter and 8-cm height, which emulated the vortex-anchored flow patterns behind the filter-feeding pattern of *E. aspergillum*.

Smoothness and uniformity of flow field. Flow pattern is vital for dynamic oil cleanup using adsorbents. To examine the flow pattern at adsorption region on a quantitative basis, we compared six kinds of skeleton architectures (Fig. 1c), i.e., solid plate (SP), solid cylinder (SC), grid hollow cylinder (GC), chequerboard hollow cylinder (CC), helical ridge-grid hollow cylinder (HC), and bio-inspired hollow cylinder (BC) skeleton, with details of these geometries given in Supplementary Text 2. For each skeleton architecture, the velocity (V , cm s^{-1}) and pressure (P , Pa) field were modeled at Re value of 10^2 , 10^3 , 10^4 and 10^5 . The flow field analysis was conducted on a horizontal cross-section at the mid-height of VAF. The adsorption region was the cavity area for hollow structures, peripheral area for solid structures, circular ring for SC (outer diameter 7.08 cm, inner diameter 5 cm) and rectangular ring for SP (outer dimensions 3.36×7.36 cm, inner 1×5 cm). This setup enabled equal adsorption areas (Supplementary Fig. 6). In these adsorption regions, the smoothness of flow pattern was evaluated based on the distribution of V and P at discrete nodes. In addition, the uniformity was assessed by the coefficient of variation (CV) for V and P where dimensionless CV was defined as the ratio of standard deviation to mean value²⁴. A larger absolute value of CV means a greater dispersion for data distribution.

We summarized the magnitude of velocity and CV_v surrounding the adsorbent under different Re values. As shown in Fig. 1e, the BC skeleton with open pores reduced the velocity by almost one order of magnitude compared with that for SC and SP skeletons. Even for $Re=10^5$ ($V=350 \text{ cm s}^{-1}$) in supercritical regime, the BC could still attenuate turbulence with velocity decay to the level as low as 23 cm s^{-1} inside the cavity, indicating minimal disturbance to flagellum-shaped adsorbent. The velocity reduction is attributed to the interlaced fluid-alleyways and high-permeability pore network²⁵, which prevented the flow from being accelerated when passing the cylinder or plate structures. In addition, much more uniform velocity field was obtained for BC compared with that for SC and SP skeletons, even in supercritical regime. For example, when Re value was increased from 10^2 to 10^5 , the CV_v for SC skeleton was increased from 0.8 to 1.5, implying discrete and non-uniform velocity distribution (Fig. 1e and Supplementary Fig. 7). In contrast, the BC exhibited a substantially more uniform velocity, with CV_v being as low as 0.15 (Supplementary Fig. 7). Likewise, uniform flow field was not achieved for other hollow skeletons (i.e., GC, CC and HC), because disassembling the helical ridge and chequerboard lattice resulted in a significant loss of reversing streamline in the half space of cavity (Fig. 1d). This led to an almost 3-fold increase in CV_v for CC (0.5) and HC (0.4) compared with that for BC (Supplementary Fig. 7). This suggested the smooth and uniform flow field via vortex-anchored mechanism for *E. aspergillum*.

The BC skeleton exhibited a vortex-induced negative pressure distribution inside the cavity (Fig. 1f), which physically attracted oil to move onto the adsorbent. In comparison, the SP and SC structures produced both positive and negative pressures, potentially leading to insufficient oil-solid contact and inefficient usage of the adsorbent materials. Because the pressure field included both positive and negative values, we used the absolute value of CV_p to describe the uniformity of the flow field. Compared with the discrete pressure distribution around SC with $|CV_p|=78.2$ for $Re=10^2$ and 3.0 for $Re=10^5$, respectively, uniform pressure distribution was observed for BC ($|CV_p| < 0.2$). Replacing BC skeleton motif by other hollow structures (i.e., GC, CC and HC) resulted in sparse vortices and non-uniform pressure distribution ($|CV_p| > 1.0$; Fig. 1f and Supplementary Fig. 8). Hence, combination of helical ridge and chequerboard lattice learned from *E. aspergillum*'s skeletal motif created a suitable hydrodynamic condition

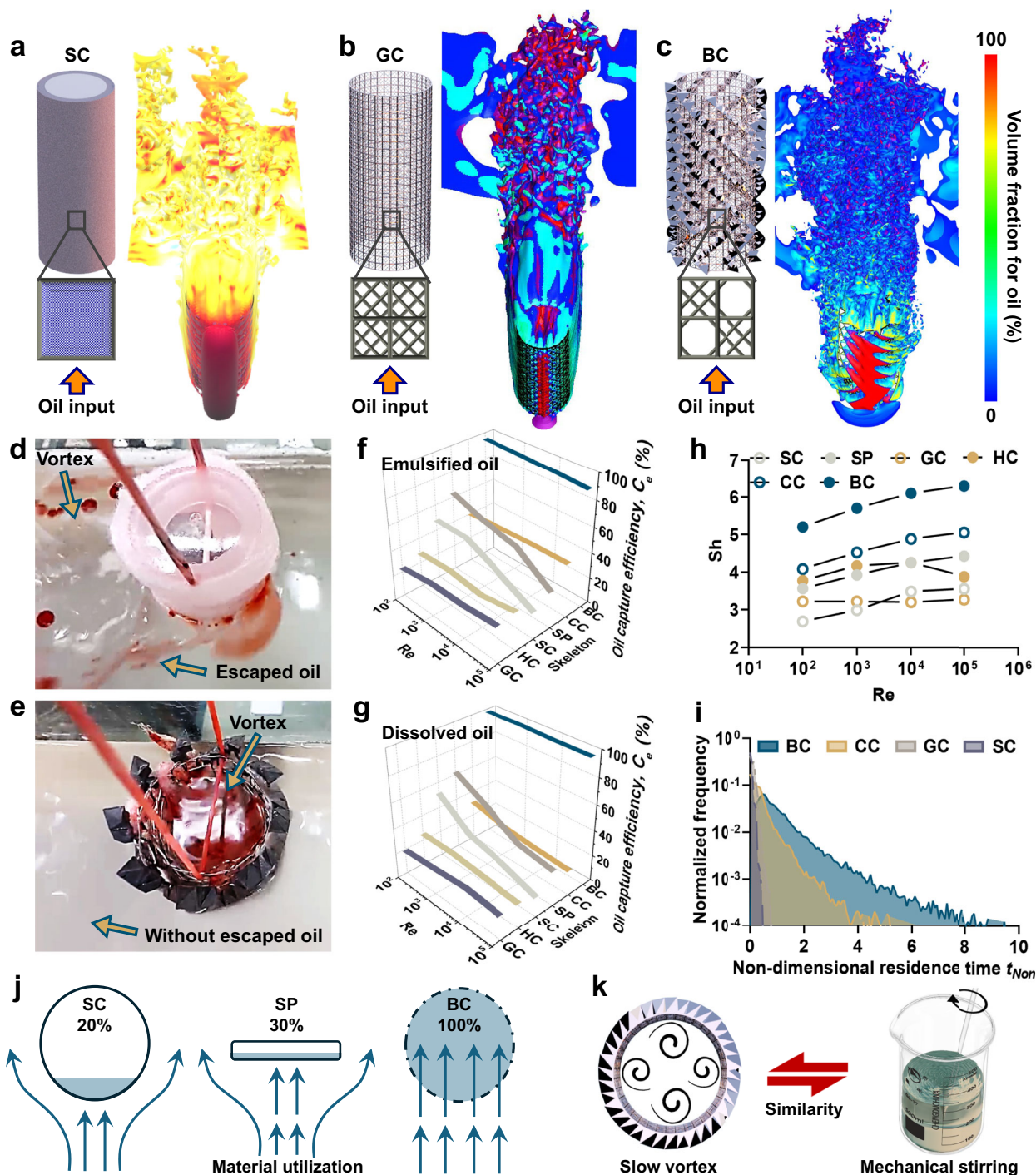


Fig. 2 | Comparison of mass transfer for different skeletons. **a–c** Volume fraction of emulsified oil at the wake flow for **(a)** solid cylinder (SC), **(b)** grid hollow cylinder (GC) and **(c)** bio-inspired hollow cylinder (BC) skeleton. **d, e** Optical images of oil distribution for **(d)** SC skeleton and **(e)** BC skeleton. **f, g**, Simulated oil capture

efficiency (C_e) for **(f)** emulsified and **(g)** dissolved oil. **h** Simulated Sherwood number (Sh). **i**, Dimensionless residence time (t_{Non}) at supercritical regime. **j** Simulated Material utilization (M_U). **k** Schematic illustration of vortex-anchored flow pattern for VAF. Source data are provided as a Source Data file.

for stable oil capture by the adsorbent over Reynolds numbers from subcritical to supercritical regimes.

Enhancement of mass transfer

We next investigated the mass transfer during oil capture by VAF under different oil-water states, i.e., dissolved oil, floating oil, and emulsified oil, for an oil volume fraction of 1%. The mass transfer pathway for floating oil was experimentally observed in a flume at water-flow velocity in the range of 0–350 cm s⁻¹, and that for dissolved and

emulsified oils were theoretically simulated by using Lattice Boltzmann method. Considering the inertial-flow effects, we simulated the mass transfer of dissolved and emulsified oils at $Re=10^2, 10^3, 10^4$ and 10^5 based on single-phase flow and multi-phase flow modeling²⁶, respectively (Method and Supplementary Text 3).

Fig. 2a–e show the pattern of mass transfer for floating and emulsified oils. Based on modified Shan-Chen algorithm developed by Falcucci et al.^{27,28} and Dollet et al.²⁹ who used both repulsive and frustration forces to stabilize the droplets, the simulation could

accurately capture droplet distribution in the wake region. Unlike the SC and SP structures around which oil droplets bypassed and flowed away, negative hydrodynamic pressure driven by vortical flow in the cavity of BC directly attracted the oil droplets for enhancing oil-solid interfacial contact. This appeared to be in line with the attraction of buoyant particles towards vortices reported by Fujiki et al.³⁰. This suction effect accounted for almost 100% utilization for adsorbents (Fig. 2d, j), compared with that of 30% for SP and 20% for SC, respectively (Fig. 2e, 2j and Supplementary Fig. 9). As a result, the BC was found to capture more than 97% of emulsified and floating oil at each Re value, with <3% being leaked into the quiescent region downstream (Fig. 2f). In contrast, the capture efficiency for SC was lower than 54% at Re=10², and the values were further declined to 46% at Re=10³ and 22% at Re=10⁵. That is, BC could be highly resistant to water-flow fluctuation over a wide Re number ranging from subcritical to supercritical regions. Owing to non-uniform distribution of vortex field and negative pressure, GC, CC, and HC without helical ridge or chequerboard lattice were shown to capture only 27–32%, 43–47% and 30–35% of emulsified oil at Re=10²–10⁵ (Fig. 2f).

To quantify the mass transfer of dissolved oil, we calculated the Sherwood number (Sh) in accordance to inner concentration field of dissolved oil (Eq. 9). Sh value obtained for BC (5–6) filled with vortices was approximately two folds of that obtained for SP (3.3–4) and SC (2.5–3.5; Fig. 2h). This accounted for capture efficiency of 98% obtained for BC at Re=10⁵, the value being 4-fold and 6-fold of that observed for SP (28%) and SC (16%), respectively (Fig. 2g). These results suggested enhanced mass transfer by extra inertia effect associated with the uniform vortex-anchored field inside BC cavity of VAF whose oil cleanup was independent on oil-water states. For other hollow skeletons without helical ridge and chequerboard lattice (i.e., GC, CC, and HC), there was no extra inertial effect requisite for preventing dissolved oil from escape. Thus, the capture efficiencies for GC, CC, and HC were decreased to lower than 30% even for subcritical regime (Re=10² and 10³) (Fig. 2g), which were even lower than that for SP and SC. This clearly demonstrated vortex-anchored flow pattern to be responsible for enhanced mass transfer and oil capture.

Additionally, residence time is another essential factor that exerts major influence on mass transfer and adsorption delay³¹. We further derived dimensionless residence time from vorticity field according to Eq. 11, as a measure of the time available for oil to dwell within the skeleton cavity. Figure 2i and Supplementary Fig. 10 show the normalized frequency for each non-dimensional residence time (t_{Non}). Compared with SC whose maximum t_{Non} was shorter than 1.6 at Re=10⁵, BC exhibited an order of magnitude increase in maximum t_{Non} (9.8). This phenomenon could be further supported by the slow vortex field observed in both optical images (Fig. 2d) and simulated flow fields (Fig. 1d). The maximum t_{Non} observed for CC, GC and HC was only 5.3, 2.6 and 2.3, respectively, indicating the dependence of residence time on vortex-anchored flow pattern associated with helical ridge and chequerboard lattice. Notably, such mass transfer mechanism was fundamentally applicable by analogy to the stirring frequently observed for beakers in laboratory³². That is, the VAF with BC skeleton shifted the mass transfer from conventional macro-scale intercept mode to in-situ stirring mode driven by discrete small-scale vortex.

Hydrodynamic robustness

Hydrodynamic stability holds the key to robust oil cleanup under complex water-flow environments. The loss in hydrodynamic stability not only leads to inflexible and imprecise operation but also irreversibly lower mass transfer and oil capture efficiency³. We examined the hydrodynamic stability in terms of pressure drop (ΔP), drag coefficient (D_c) and experimentally measured swing angle (θ_{sw}) of different matrixes in the flume shown in Fig. 3a at Re=10²–10⁵. To decouple the impact of rotational inertia, each skeleton was designed with identical

weight, size, and loading mode during the tests, as detailed in the Method section and Supplementary Fig. 11.

The BC structure remains stably vertical across subcritical, critical, and supercritical flow regimes due to lower pressure drop (ΔP) and reduced drag coefficient (D_c) (Fig. 3b). In detail, variation of ΔP for BC (0.007–800 Pa) was at least one order of magnitude smaller than that for the solid SC skeleton (0.3–5000 Pa) as Re was increased from 10² to 10⁵ (Fig. 3c). Thus, the BC exhibited the most remarkable drag reduction, indicated by a D_c value as small as 1.2–0.4, which was almost half of that for SC (1.8 to 1.6) (Fig. 3d). In contrast, the higher D_c and ΔP led the solid SC to sway by $\theta_{sw}=20^\circ$ (Re=10²) to $\theta_{sw}=50^\circ$ (Re=10⁵) along the flow direction (Fig. 3b, e). Notably, the vortex shedding behind the SC was apparently visible under turbulent flow (Re=10⁴–10⁵; Movies S1–S3).

We next investigated the impact of skeletal motifs on hydrodynamic robustness of hollow-structured skeletons. As shown in Fig. 3c, the skeletons without chequerboard lattice (i.e., GC and HC) were subjected to much higher ΔP (0.08–5000 Pa) compared with that of CC (0.005–700 Pa) and BC (0.007–800 Pa) for all Re values. This led to the re-rise in drag for the GC and HC, especially for strong turbulent flow (Re=10⁴–10⁵), indicated by D_c of GC and HC being higher than 1.5 (Fig. 3d). Thus, these simple grids were not able to achieve stable hydrodynamic responses during oil capture. Removing helical ridge from BC resulted in a slight decrease in D_c for CC by an amplitude of 0.1, suggesting the insignificant contribution of helical ridge to fluid resistance of VAF (Fig. 3d). However, such minor impact on D_c was unlikely to compromise the hydrodynamic robustness, as BC was always kept vertical and stable under all tested Re (Fig. 3b). Considering the structural stability benefited from the helical ridge plus enhanced mass transfer, the trade-off between hydrodynamic robustness, mass transfer and structural stability could be well addressed for BC under laminar, transition and turbulent flow conditions.

Hydrodynamic mechanisms

We next elucidated the mechanisms that enabled mass transfer and hydrodynamic robustness of BC inspired by the predation strategy of *E. aspergillum*. Our previous study verified that the vortices could reduce the intersection angle between velocity vector and concentration gradient, thereby physical field synergy was realized for enhanced mass transfer³³. Thus, we hypothesize that the vortex-anchored mechanism was also responsible for the excellent performance obtained for BC within the context of physical field synergy.

To verify this hypothesis, we first examined the relationship between vorticity field, Sh value and physical field synergy (Supplementary Text 4 and Fig. 4a, b). For all the six structures tested herein, high vorticity implied small local synergic angle (θ_s) for water flow surrounding the adsorbents (Fig. 4a). Moreover, the Sh value was positively correlated with the volume-weighted average θ_s (i.e., volumetric average synergic angle, θ_v). As θ_v was declined from 65° to 15°, Sh was increased from 3 to 7.5 for BC under all the Re values (Fig. 4c). This offered the most likely explanation to the reason for enhanced mass transfer by modifying flow pattern to achieve physical field synergy.

We next assessed the field synergy of different skeletons. For solid SC, the vortex with $\theta_s < 45^\circ$ tended to form behind the skeleton at a large Kolmogorov microscale (K_m)³⁴ of 425 μm where oil was difficult to access due to flow deflection (Fig. 4a and Supplementary Fig. 12). Although $\theta_s < 45^\circ$ accounted for approximately 30% of the total adsorption sites (Fig. 4d), the SC was subjected to ineffective mass transfer at supercritical flow (Re=10⁵). On the contrary, the BC evoked remarkably uniform distribution of vortices at small K_m of 85 μm within the cavity, allowing 70% of total adsorption regions with small θ_s (<45°) from laminar to turbulent flow environments. This difference provided a plausible explanation for the higher mass transfer of BC

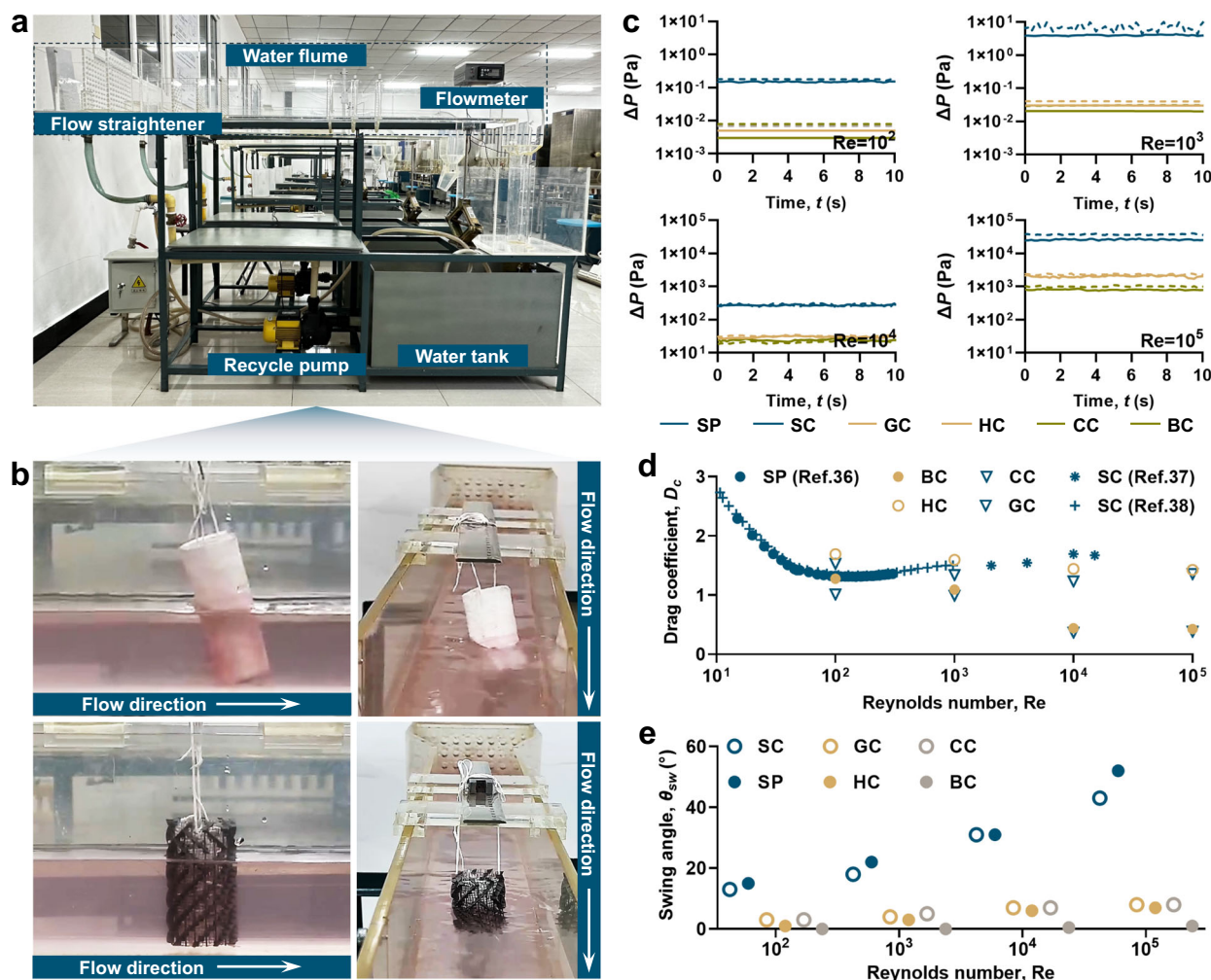


Fig. 3 | Comparison of hydrodynamic robustness. **a** Optical images of velocity flume. **b** Posture of solid cylinder (SC) and bio-inspired hollow cylinder (BC) skeletons under supercritical regime at $Re=10^5$ (Supplementary Movies 1–4).

c Simulated pressure drop (D_p). **d** Simulated drag coefficient (D_c). **e**, Measured swing angle (θ_{sw}) over subcritical, critical and supercritical regimes. Source data are provided as a Source Data file.

owing to more sufficient adsorbent utilization in comparison with SC during water-flow transitions. On the other hand, inside the hollow skeletons without chequerboard lattice (i.e., GC and HC), there was no observation of apparent vortex and small θ_s ($<45^\circ$) regions over all the Re values (Figs. 4a, 4d and Supplementary Figs. 13–15), suggesting the importance of chequerboard-like structure for vortex formation and realization of physical field synergy. For hollow skeletons with chequerboard lattice but lacking helical ridge (i.e., CC), vortices with $259 K_m$ were only generated in the front half of cavity. In this case, poor mass transfer was encountered in the latter half part with only 25% small- θ_s regions ($\theta_s < 45^\circ$) that occurred under supercritical regime (Supplementary Figs. 13–15). The current study shows that mass transfer was enhanced inside the BC cavity by the slow vortex field and physical field synergy driven by synergistic contribution of chequerboard lattice and helical ridge, beyond the previously known benefit of increased residence time¹⁶.

Next, mechanistic insights into drag reduction were also elucidated by modeling the hydrodynamic field downstream through monitoring the velocity fluctuation and Reynolds stresses (Rs) at three Cartesian directions at the center of recirculation region (point A) of cylinder wake (Fig. 4a). This point A was located at the symmetry axis of skeletons along the flow direction, and $2.5D$ downstream from the skeleton (D is the diameter of BC). Figure 4e–g reveal the final -1% of time evolution within the statistical steady state of the given fluid

regime. As fluid alleyways penetrated into the recirculation region, two solid skeletons (i.e., SC and SP) were characterized by intense velocity fluctuation and high Rs at all three directions³⁵, ranging from -180 to 200 cm s^{-1} and 1.3 – 4.4 kPa , respectively. By contrast, even at supercritical flow (i.e., $Re=10^5$), the helical ridge of BC disturbed the recirculation in wake flow (Fig. 4a and Supplementary Figs. 17) and exhibited negligible fluctuation at point A with velocity components nearly approaching constant 0 cm s^{-1} , leading Rs to be only 0.002 – 0.04 kPa . This clearly demonstrated the capability of BC to stabilize the flow field, thereby both pressure drop and drag could be sustained quasi-statically. Moreover, other hollow skeletons without chequerboard lattice (i.e., GC) failed to avert unstable recirculation in wake flow in three-axis velocity directions (fluctuation amplitude of -120 to 180 cm s^{-1} , Rs of 1.3 – 1.9 kPa ; Fig. 4e–g and Supplementary Fig. 18). Those with chequerboard lattice but without helical ridge (i.e., CC) were found to only stabilize the velocity and Rs in the vertical direction, whereas fluctuation in horizontal direction remained as great as -100 to 100 cm s^{-1} and 0.06 – 0.7 kPa (Fig. 4e–g). That is, only BC had the capability of wake stabilization among all the structures tested herein.

To shed light on mechanistic insights into such hydrodynamic behavior, we examined the evolution of flow pattern with respect to increased complexity of skeleton from simple grid structure (GC) to complex BC structure. Compared with GC across which all streamlines

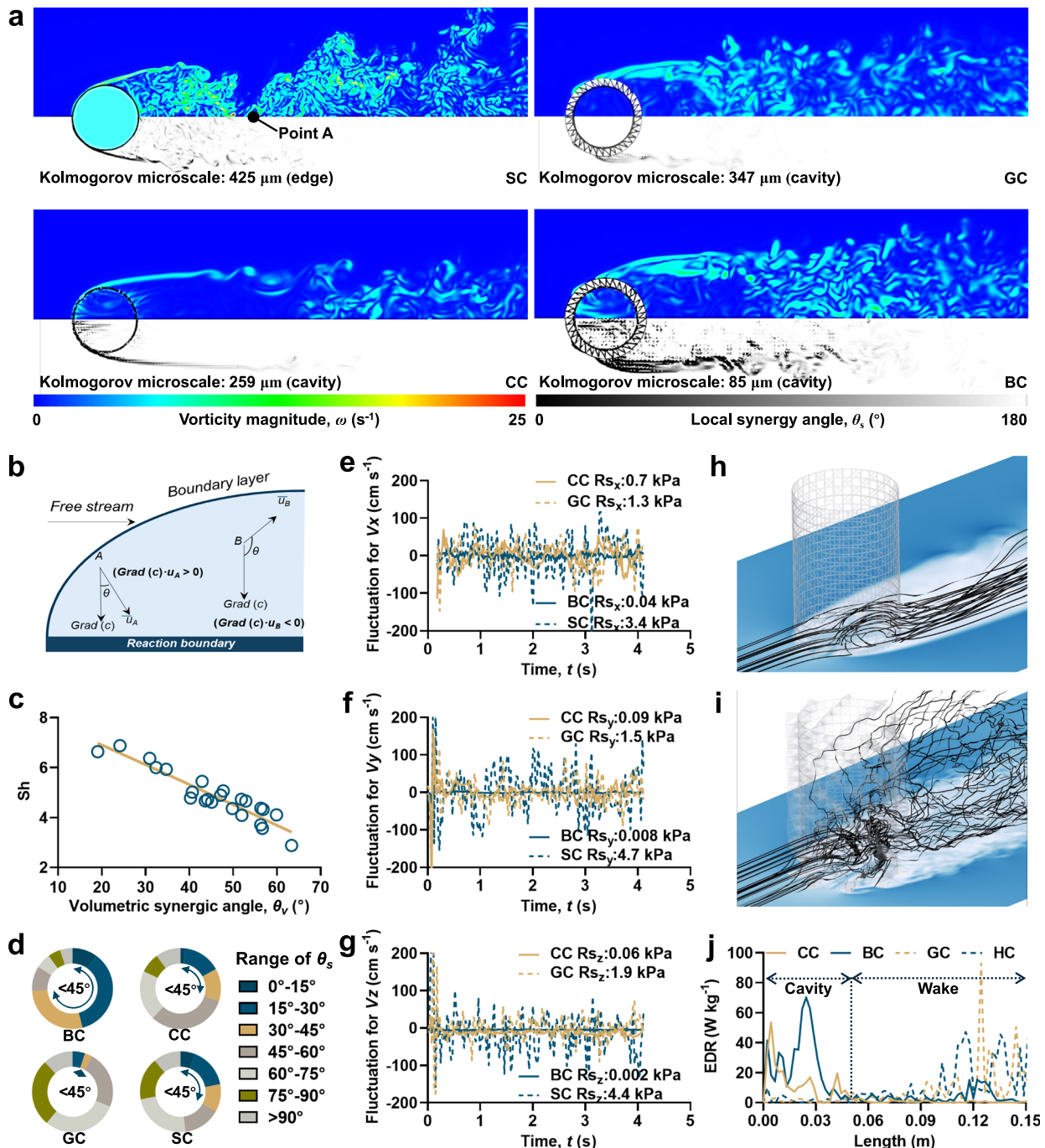


Fig. 4 | Effect of skeletal morphology on flow pattern, field synergy, and energy dissipation at $Re=10^5$. **a** Vorticity and local synergic angle (θ_s). **b** Schematic illustration of physical field synergy. **c** Relationship between Sh and volumetric synergic angle (θ_v). **d** Proportion of local synergic angle (θ_s). **e–g** Time evolution of velocity fluctuation and Reynolds stresses (Rs) at point A under (e) x component, (f) y component and (g) z component. Zoomed-in view of streamline for (h) bio-inspired

hollow cylinder (BC) and (i) chequerboard hollow cylinder (CC) skeletons. **j**, Energy dissipation rate (EDR, $W\ kg^{-1}$) was calculated by velocity distribution along flow direction according to Eq. 12. As shown in Fig. 4j, the kinetic energy of turbulent flow was converted to rotational energy with the EDR of $20\text{--}70\ W\ kg^{-1}$ inside BC cavity for $Re=10^2\text{--}10^5$, thereby EDR was decayed to $0\text{--}5\ W\ kg^{-1}$ in the quiescent region downstream (Fig. 4j and

traversed the cavity directly (Supplementary Fig. 19), abundant vortices were generated via more intensive interaction and reversion of streamlines behind the chequerboard lattice of CC (Fig. 4h). The reversing streamlines resulted from the difference in orientation and velocity of water flow in 2D plane induced by multi-angle struts²⁵ of chequerboard lattice (Fig. 4h). Nonetheless, the streamline reversal disappeared in the latter half of CC cavity led to insufficient distribution of vortices (Fig. 4h). Vertical guidance for the streamlines employed by helical ridge allowed them to collide, deflect, converge

and separate in broader 3D space (Fig. 4i). As a result, the BC reinitiated the missing streamline reversal, followed by creating the low-speed and small scale (K_m of $85\ \mu m$ at supercritical regime) vortices that filled the cavity extensively (Fig. 4i). Furthermore, energy dissipation rate (EDR, $W\ kg^{-1}$) was calculated by velocity distribution along flow direction according to Eq. 12. As shown in Fig. 4j, the kinetic energy of turbulent flow was converted to rotational energy with the EDR of $20\text{--}70\ W\ kg^{-1}$ inside BC cavity for $Re=10^2\text{--}10^5$, thereby EDR was decayed to $0\text{--}5\ W\ kg^{-1}$ in the quiescent region downstream (Fig. 4j and

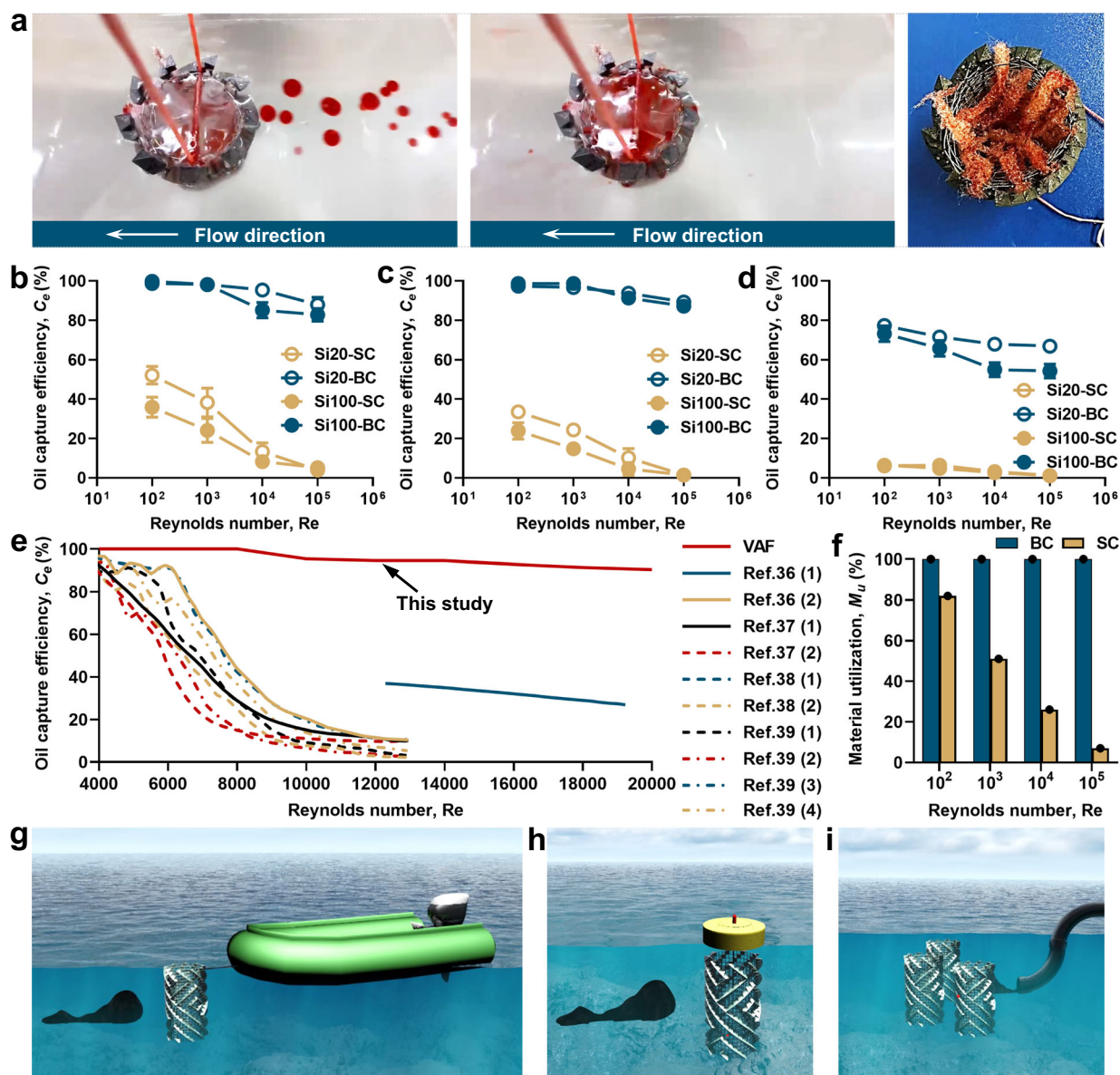


Fig. 5 | In-situ oil cleanup and potential applications. **a** Robust oil cleanup by vortex-anchored filter (VAF) at $Re=10^5$. **b–d** Effect of oil viscosity and Re number on C_e for (b) floating oil, (c) underwater oil and (d) emulsified oil. **e** Floating-oil capture efficiency as function of Re by making comparison with reference data for oils with viscosities of 39.3–111.9 mPa·s (i.e., ISO 32, SAE 5W-20, SAE 5W-30, SAE 10W-40, SAE

15W-40). **f** Comparison of material utilization (M_u) between solid cylinder (SC) and bio-inspired hollow cylinder (BC) skeletons. **g–i** Three typical application of VAF for (g) flexible oil cleanup integrated to mobile vehicles, (h) real-time cleanup by serving as ballast for buoys and (i) vertical barrier for long-term cleanup at source. Source data are provided as a Source Data file.

Supplementary Fig. 20). Notably, for solid skeletons and simple-grid structures (CG and HC), high-EDR regions were found to be located in the wake flow ($25\text{--}90\text{ W kg}^{-1}$) rather than in the cavity ($5\text{--}15\text{ W kg}^{-1}$) over a wide Re numbers. This resulted in considerable performance loss in terms of hydrodynamic stability and mass transfer. Taken together, the chequerboard grid was likely to be essential for generating vortices in the 2D plane, while the helical ridge played the role of reconstructing flow velocity, vortex scale, and vortex distribution in the 3D space. Our results highlighted the importance of helical ridge and the chequerboard lattice for dissipation and redistribution of water-flow energy, which was in good consistence with that reported in previous studies on biophysical mechanisms for hydrodynamic stability offered by *E. aspergillum*¹⁸. Physical field synergy provided the most likely explanation for the reason why enhanced mass transfer and filter-feeding efficiency were improved by vortex-anchored flow pattern.

Oil cleanup by VAF under turbulent flow

To further verify the applicability of VAF for dynamic robust cleanup of spilled oil, we performed experimental investigations on capture efficiency (C_e) for floating oil, underwater oil and emulsified oil with Si100 and Si20 (e. g. silicone oil) under $Re=10^2\text{--}10^5$ (Method). The results obtained for floating oil were compared with those reported in previous studies^{8,36–38}, and those for underwater and emulsified oils were compared with the SC matrix.

The capture of floating oil, underwater oil and emulsified oil is illustrated by using VAF (Fig. 5a) and conventional interception matrixes (Supplementary Fig. 9). The SC matrix was unable to adsorb all three kinds of oils immediately, i.e., adsorption delay^{1,7}, and the oil was aggregated to dispersed droplets on the surface of adsorbent (Supplementary Fig. 12). In comparison, these oils could be retained and anchored by low-speed small-scale vortices generated in the cavity of VAF matrix (Fig. 5a), which prevented secondary leakage. As a result,

the SC device only captured 50% of floating Si20, 40% of underwater Si20, and only 7% of emulsified Si20 even under laminar flow ($Re=10^2$; Fig. 5b-d). Under strong turbulent flow ($Re=10^5$), these values were further declined to 7%, 5% and 1%, respectively, as a consequence of oil escape via streamline deflection. With increase in oil viscosity (Si20-Si100, 19–97 mPa s), the SC device only captured 40% of floating Si100, 21% of underwater Si100, and 6% of emulsified Si100 at $Re=10^2$, indicating the sensibility to adsorption delay. In fact, the C_e did not exceed 90% for conventional interception based on similar SC and SP skeletons, unless the Re was lowered down to 5000 ($V < 17 \text{ cm s}^{-1}$; Fig. 5e)^{8,36–38}. Remarkably, the VAF demonstrated the excellent performance for capturing all the types of oil with efficiency higher than 97% (Fig. 5b-d), even at supercritical regime ($Re=10^4$ and 10^5). More importantly, the adsorbent utilization reached almost 100% during oil-cleanup (Fig. 5f) in favor of enhanced mass transfer and long residence time. Taken together, the VAF demonstrated capability of dynamic robust oil cleanup by alleviating adsorption delay, oil escape and hydrodynamic instability over subcritical, critical and supercritical regimes.

We also tested the C_e of VAF for crude oil with much higher viscosity of 1200 mPa·s. At room temperature (25 °C), $C_e < 10\%$ was observed due to blockage of the pores by paste-like, low-fluidity crude oil. When the crude oil was dispersed into droplets by raising temperature to 65°C and stirring, C_e could reach 80% for all the Re values (Supplementary Fig. 21). This necessitated the coupling of VAF to heating process (e. g. photothermal or electrothermal module) for capture of crude oil.

In light of above results, the bio-inspired VAF can be applied for dynamic robust cleanup of spilled oil with adaptability, flexibility and sustainability in several practically relevant scenarios. For example, the VAF can be well-suited to be integrated to mobile vehicles such as boat and ship, which realizes real-time decentralized pinpoint-positioning cleanup of floating, underwater and emulsified oils wherever they are spilled (Fig. 5g). In addition, the VAF can find application by serving as ballast for buoys, which allows timely cleanup in quick response to accidental oil-spill emergencies (Fig. 5h). Moreover, by virtue of superior hydrodynamic robustness and permeability, VAFs can be also used in interconnected way so as to build up long-term vertical barriers that accomplish prevention of oil spill at source (Fig. 5i). The VAF could be operated in a stationary position in turbulent flow, or positioned at the front or rear of a vessel by optimizing geometric configuration, materials and connections. For practical applications, the scale-up of VAF could be achieved by two modes, i.e., (i) principle of similarity based on relevant similarity criterions such as Reynolds number (Re), Euler number (Eu), Weber number (We) and Sherwood number (Sh), and (ii) numbered-up strategy to make scalable arrays by increasing the quantity of VAF modules (Supplementary Text 5).

From the life-cycle point of view, the devices after oil capture need to be disposed properly^{1,3}. Hence, building-block assembly of VAF allows the used flexible adsorbents to be recycled, and the rigid skeleton to be reused by simply replacing new adsorbents. In the meantime, adsorbed oil together with the flagellum-adsorbent can be treated in the centralized manners such as burning, recycling and landfill. Cyclic tests validated the retrievability of both adsorbent materials and oil (Supplementary Fig. 23). Compared with commercial booms, skimmers, and chemical methods for oil-cleanup, the VAF developed by bio-inspired vortex-anchored flow pattern demonstrates several advantages for in-situ, dynamic robust oil cleanup under turbulent flow. This study provides insights into biophysically inspired development of all-in-one strategies for cleanup of spilled oil, benefiting from flexibility and adaptability, easy-to-handle operability and scalability, environmental compatibility and life-cycle sustainability.

Discussion

Drawing inspiration from skeletal features and filter-feeding patterns of deep-sea glass sponge *E. aspergillum*, we developed a vortex-anchored filter (VAF) that was practically applicable for in-situ, dynamic and robust oil cleanup under complex hydrodynamic conditions. The VAF could retain external turbulent-flow kinetic energy in small-scale low-speed vortical flow, leading to enhanced interfacial mass transfer by physical field synergy beyond previously known residence time increment. It improved hydrodynamic stability by attenuating the Reynolds stresses in wake flow. The VAF was able to realize >97% capture of floating, emulsion and dissolved oil over subcritical, critical and supercritical regimes, even under strong turbulent flow ($Re=10^5$). The present interdisciplinary study lies on the interface of environmental engineering, fluid mechanics, biophysics and bio-nics, which not only highlights the importance of hydrodynamics for oil capture, but also represents a paradigm shift to advance biophysically inspired strategies for in-situ, dynamic and robust cleanup of spilled oil. Besides that, our work will have broader implications that extend to bio-inspired design for advanced systems coupled with photothermal, electrothermal and electrochemical modules that are more applicable, more economical and more sustainable for environmental remediation^{39,40} and resource recovery⁴¹ under practically relevant hydrodynamic conditions.

Methods

Modeling

To model velocity, pressure and oil volume fraction during oil cleanup, 3D Shan-Chen multi-component lattice Boltzmann framework was developed on the basis of four assumptions: (i) the solid phase was stationary and non-deformed, (ii) the fluid phase satisfied no-slip condition at the fluid-solid interface, (iii) the computational domain was saturated by fluid components without air, and (iv) the oil droplet trajectory terminated when intercepting the adsorption region⁴². The dynamics of two-phase fluid were modeled by using the entropic lattice Boltzmann (ELBM) method⁴³, accounting for both momentum conservation and continuity equation. Interaction between oil and water phase was described by the Shan-Chen pseudopotential approach, and the Shan-Chen force was coupled in source term^{26,29}.

$$f_i^k(\mathbf{s} + \mathbf{c}_i \Delta t, t + \Delta t) = f_i^k(\mathbf{s}, t) + \alpha \beta [f_i^{k,eq}(\rho, \mathbf{V}) - f_i^k(\mathbf{s}, t)] + [f_i^{k,eq}(\rho, \mathbf{V} + \Delta \mathbf{V}) - f_i^{k,eq}(\rho, \mathbf{V})] + \mathbf{F}^k(\mathbf{s}) \quad (1)$$

$$f_i^{k,eq} = \rho^k w_i \left[1 + \frac{\mathbf{c}_i \cdot \mathbf{V}}{c_s^2} + \frac{(\mathbf{c}_i \cdot \mathbf{V})^2 - \mathbf{V} \cdot \mathbf{V}}{2c_s^4} + \frac{(\mathbf{c}_i \cdot \mathbf{V})^3 - 3(\mathbf{c}_i \cdot \mathbf{V})(\mathbf{V} \cdot \mathbf{V})}{6c_s^6} \right] \quad (2)$$

$$\mathbf{F}^k(\mathbf{s}) = -\frac{G_{AB}}{\rho_0^k} \rho^k(\mathbf{s}) \sum_{i=1-18} w_i (|\mathbf{c}_i|^2) \rho^k(\mathbf{s} + \mathbf{c}_i) \mathbf{c}_i - G_{AA,1} \psi^k(\mathbf{s}) \sum_{i=1-18} w_i (|\mathbf{c}_i|^2) \psi^k(\mathbf{s} + \mathbf{c}_i) \mathbf{c}_i - G_{AA,2} \psi^k(\mathbf{s}) \sum_{i=1-54} p_i (|\mathbf{c}_i|^2) \psi^k(\mathbf{s} + \mathbf{c}_i) \mathbf{c}_i \quad (3)$$

where $f_i^k(\mathbf{s}, t)$ was the probability density function for component k (i.e., water or oil) at site \mathbf{s} and discrete time t (s), moving along the i th lattice direction; \mathbf{c}_i (cm s^{-1}) the lattice velocity vectors; Δt (s) the time step; α the characteristic collision frequency calculated by entropy minimization (see details in Eq. 4); $0 < \beta < 1$ a parameter related to the fluid's kinematic viscosity ν_k ($\text{cm}^2 \text{ s}^{-1}$), defined as $\nu_k = (\beta^{-1} - 1)c_s^2/2$; $f_i^{k,eq}$ the local Maxwellian equilibrium, expressed as a third-order Mach-number expansion of the continuum Maxwell-Boltzmann distribution; w_i the weights associated with each lattice velocity direction; c_s the speed of sound within the lattice framework (commonly $3^{0.5}$ in lattice units)²⁶; ρ^k the hydrodynamical densities for both components defined as, $\rho^k = \sum_i f_i^k$; \mathbf{V} the macroscopic velocity given by $\mathbf{V} = (\sum_k, i f_i^k \mathbf{c}_i) / (\sum_k \rho^k)$; $\mathbf{F}^k(\mathbf{s})$ the

modified Shan-Chen model that included repulsive and frustration forces; G_{AB} the interaction strength parameter for repulsive force between two components; $G_{AA,1}$ and $G_{AA,2}$ the interaction strength parameters for short-range self-attraction and long-range self-repulsion within a single component, respectively; p_i the weights associated with each lattice velocity direction for long-range self-repulsion; ψ^k the pseudopotential function given by $\psi^k(\mathbf{s}) = \rho_0(1 - e^{-\rho^k(\mathbf{s})/\rho_0})$; ρ_0 the reference density. Detailed description could be found in refs. 26,29,43.

The parameter α in Eq. 1 was key to maintaining the entropy balance in the relaxation step at each node and could be obtained as the nontrivial root of the equation.

$$H[f_i^k + \alpha(f_i^{k,eq} - f_i^k)] = H(f_i^k) \quad (4)$$

where $H = -\sum_i f_i^k \ln(f_i^k/w_i)$.

For single-phase flow with dissolved oil, the discrete Boltzmann equation with single relaxation time (SRT) was

$$f_i(\mathbf{s} + \mathbf{V}_i \Delta t, t + \Delta t) = f_i(\mathbf{s}, t) - \frac{1}{\tau_f} (f_i - f_i^{eq})(f_i, \mathbf{s}, t) \quad (5)$$

$$g_i(\mathbf{s} + \mathbf{V}_i \Delta t, t + \Delta t) = g_i(\mathbf{s}, t) - \frac{1}{\tau_g} (g_i - g_i^{eq})(g_i, \mathbf{s}, t) \quad (6)$$

$$f_i^{eq} = w_i \sum_i f_i \left[1 + \frac{\mathbf{c}_i \cdot \mathbf{V}}{c_s^2} + \frac{(\mathbf{c}_i \cdot \mathbf{V})^2}{2c_s^4} - \frac{3(\mathbf{V} \cdot \mathbf{V})}{2c_s^2} \right] \quad (7)$$

$$g_i^{eq} = w_i \sum_i g_i \left(1 + \frac{\mathbf{c}_i \cdot \mathbf{V}}{c_s^2} \right) \quad (8)$$

where $f_i(\mathbf{s}, t)$ and $g_i(\mathbf{s}, t)$ were the probability density function for fluid and dissolved oil, respectively; f_i^{eq} and g_i^{eq} the local Maxwellian equilibrium; τ_f and τ_g the relaxation time related to fluid's kinematic viscosity ν_k ($\text{cm}^2 \text{s}^{-1}$) and dissolved oil's diffusion coefficient D ($\text{cm}^2 \text{s}^{-1}$), defined as $\nu_k = c_s^2(\tau_f - 0.5)\Delta t$ and $D = c_s^2(\tau_g - 0.5)\Delta t$.

Equations 1–4 were used to address two-phase flow problems, including the oil capture efficiency and oil phase distribution. Equations 5–8 were applied to single-phase flow problems, covering analysis of flow pattern, mass transfer, and field synergy. The simulation was performed by using LBMPY and waLBerla⁴⁴. All the coefficients were obtained from the software (Supplementary Table 1). We employed 19 discrete speed ($i = 0, \dots, 18$) scheme along the three spatial dimensions, which was also known as D3Q19 lattice. Standard bounce-back procedure was used to deal with the coupling between fluid and solid (i.e., skeleton and flagellum-shaped adsorbents). The details in the method were described in the prior literatures⁴⁵. More detailed descriptions on structure construction and initial/boundary conditions were available in Supplementary Text 3.

Design and construction of VAF

The VAF with BC skeleton was fabricated by using 3D printing on a commercially available machine EOS M290 (EOS GmbH, Germany) equipped with a maximum 400 W single-mode ytterbium fiber laser. Fabrication was carried out at laser power of 370 W, scanning speed of 650 mm s^{-1} , hatching space of 0.11 mm, and layer thickness of 30 μm . The build chamber was maintained at a low oxygen content (<0.1 vol%) by aerating with Argon gas. Subsequently, the samples were carefully separated from the build platform via a wire Electrical Discharge Machining (wire-EDM, DK 7732). Prior to uses, ultrasonic-cleaning was performed to wash off the powder residues by immersing the samples into alcohol solution (95%)³¹. The outer surface of the chequerboard

hollow cylinder was coated with photosensitive resin to prevent structural damage and abrasion during installation.

Oil capture tests

The oil capture and hydrodynamic stability were tested using an open flume that was 4 m long, 45 cm tall and 45 cm wide tilted 0° from horizontal, featuring glass sidewalls and a bottom to facilitate visualization (Fig. 3a). The water flow was generated by a pump equipped with a variable frequency at the maximum flow rate of 150 L s^{-1} and a resolution of 1.31 L s^{-1} . Flow rates were measured with a magnetic flow meter. The water depth was kept constant at $10.0 \pm 0.5 \text{ cm}$ using an adjustable tailgate. At the upstream end of the flume, the water passed through a flow straightener to reduce lateral velocities and make the velocity distribution as uniform as possible. The experimental section was located 1.5 m downstream of the flume entrance (Fig. 3b and Supplementary Fig. 9).

Prior to oil injection, we assessed the hydrodynamic stability of oil capture matrix by measuring their posture and swing angle (θ_{sw}) under $\text{Re} = 10^2 - 10^5$ at flow velocities of 0.35, 3.5, 35, and 350 cm s^{-1} . Each skeleton was suspended 2 cm above the flume's base by a flexible wire attached to a fixed point, ensuring that the skeletons were submerged in the water flow and had enough freedom to sway with the flow (Fig. 3b). During the tests, each skeleton shared the same weight (Supplementary Fig. 9) and suspension setup (Fig. 3b).

We then evaluated the oil capture under three kinds of oil-water mixture, i.e., floating oil, emulsified oil and underwater oil. The emulsified oil was prepared by using 30 min 10000 Hz ultrasound with an oil-water volume ratio of 1:99. The floating oil and underwater oil were pure oil. The three kinds of oil were dyed in red color by using Oil-Red-O at mass fraction of 1%. The oil spill source was modeled by two $1 \times 10^{-2} \text{ L}$ injection syringes located 10 cm upstream of the oil-capture device. The syringes were driven by an injection pump at a rate of $1 \times 10^{-3} \text{ L s}^{-1}$ to ensure that all the oils reached the adsorption zone without bypassing it (Supplementary Fig. 10). For floating oil, the injection syringes were located above the water surface, while for underwater oil and emulsified oil, the injection syringes were positioned 3 cm below the water surface. We recorded the weight difference of the adsorbents before and after the test to calculate the weight of oil captured (O_c).

Calculations and analysis

Derived from simulated distribution of dissolved oil, mass transfer from bulk flow to adsorbent surfaces was calculated by using Sherwood number (Sh) according to

$$\text{Sh} = \frac{\sum \mathbf{n}_i \cdot D \nabla C_i}{A_{\text{int}} (\langle C \rangle^f - \langle C \rangle^w) D} \quad (9)$$

where A_{int} (cm^2) was the mass transfer area for adsorbent (i.e., 100 cm^2 for hollow skeleton; 126 cm^2 for solid skeleton); $\langle C \rangle^f$ and $\langle C \rangle^w$ was the average in the fluid region and the adsorbent surfaces; L (0.5 cm) the characteristic length and D ($\text{cm}^2 \text{s}^{-1}$) the diffusion coefficient for dissolved oil.

Hydrodynamic resistance was quantified by calculating the drag coefficient D_c as

$$D_c = \frac{2F_{\text{drag}}}{A \rho_{\text{inlet}} V_{\text{inlet}}^2} \quad (10)$$

where F_{drag} (N) was the total drag force acting on the oil capture matrix computed at the statistically steady state along flow direction; ρ_{inlet} (g cm^{-3}) and V_{inlet} (cm s^{-1}) the fluid density and velocity at the domain inlet and A (cm^2) was the area of the transverse section being perpendicular to the fluid flow (i.e., 40 cm^2).

Non-dimensional residence time $t_{\text{Non}}^{19,28}$ and energy dissipation rate (EDR, W kg^{-1}) were calculated on the basis of flow velocity

V (cm s⁻¹) and vorticity ω (s⁻¹) as

$$t_{Non} = \frac{|\mathbf{V} \cdot \boldsymbol{\omega}| d_{path}}{u_{inlet}^2} \quad (11)$$

$$EDR = \nu_k \sum_{i,j=1}^3 \left(\frac{\partial V_i}{\partial x_j} + \frac{\partial V_j}{\partial x_i} \right)^2 \quad (12)$$

where d_{path} was the length of flow path through adsorption region. Adsorption region was defined early in Section “Smoothness and Uniformity of Flow Field” (Supplementary Fig. 6). For the hollow structure, the flow path passed through the cavity, whereas in SC, it bypassed the adsorption region (Supplementary Fig. 6). Therefore, d_{path} for hollow structure was calculated as diameter (5 cm), and for the solid structure, it was half of the outer diameter plus a quarter of the outer circumference (9.1 cm). ν_k (cm² s⁻¹) was the kinematic viscosity of water, subscript i and j the direction of flow velocity (i.e., x , y and z).

Reynolds stress (Rs) was calculated at three Cartesian directions to assess the turbulent fluctuations in wake flows³³, representing the covariance of the fluctuating velocity components as

$$R_{si} = \rho_{inlet} \left(\frac{1}{t} \int_0^t (V_i - \bar{V}_i)^2 dt \right) \quad (13)$$

where Rs (Pa) was the Reynolds stress, subscript i the Cartesian direction (i.e., x , y and z) and \bar{u} the time-averaged velocity.

Oil capture performance was evaluated experimentally in terms of capture efficiency (C_e) as

$$C_e = \frac{O_c}{O_0} \times 100\% \quad (14)$$

where O_c (g) and O_0 (g) was the weight of captured oil and the total oil, respectively.

Material utilization (M_u) was assessed from the optical images of the adsorbents before and after use as

$$M_u = \frac{A_{red}}{A_{total}} \times 100\% \quad (15)$$

where A_{red} (cm²) and A_{total} (cm²) was the area of dyed adsorbent and total adsorbent in the optical images, respectively. The areas were measured by using ImageJ software.

Data availability

The data that support the findings of this study are available within the paper and source data files. Source data are provided with this paper.

References

- Liu, Z. et al. Dual-bionic superwetting gears with liquid directional steering for oil-water separation. *Nat. Commun.* **14**, 4128 (2023).
- Yan, K. et al. High-throughput clean-up of viscous oil spills enabled by a gel-coated mesh filter. *Nat. Sustain.* **6**, 1654–1662 (2023).
- Schrope, M. Oil spill: Deep wounds. *Nature* **472**, 152–154 (2011).
- Ouda, M. et al. Novel static mixers based on triply periodic minimal surface (TPMS) architectures. *J. Environ. Chem. Eng.* **8**, 104289 (2020).
- Mallari, C. B. C. et al. Modeling oil spill disasters using system dynamics: A case study on the MT Princess Empress oil spill in Oriental Mindoro, Philippines. *Int. J. Disaster Risk Reduct.* **108**, 104524 (2024).
- Abidli, A., Huang, Y., Cherukupally, P., Bilton, A. M. & Park, C. B. Novel separator skimmer for oil spill cleanup and oily wastewater treatment: From conceptual system design to the first pilot-scale prototype development. *Environ. Technol. Innov.* **18**, 100598 (2020).
- Hoang, A. T., Nguyen, X. P., Duong, X. Q. & Huynh, T. T. Sorbent-based devices for the removal of spilled oil from water: a review. *Environ. Sci. Pollut. Res.* **28**, 28876–28910 (2021).
- Yan, X., Liu, G., Xu, J. & Ma, X. In situ oil separation and collection from water under surface wave condition. *Langmuir* **37**, 6257–6267 (2021).
- Lin, X. et al. Cobweb-inspired superhydrophobic multiscaled gating membrane with embedded network structure for robust water-in-oil emulsion separation. *ACS Sustain. Chem. Eng.* **5**, 3448–3455 (2017).
- Zhu, Q. & Pan, Q. Mussel-inspired direct immobilization of nanoparticles and application for oil-water separation. *ACS Nano* **8**, 1402–1409 (2014).
- Hofstetter, T. B. et al. Perspectives of compound-specific isotope analysis of organic contaminants for assessing environmental fate and managing chemical pollution. *Nat. Water* **2**, 14–30 (2024).
- Ali, N. et al. Robust bioinspired surfaces and their exploitation for petroleum hydrocarbon remediation. *Environ. Sci. Pollut. Res.* **29**, 61881–61895 (2022).
- Divi, R. V., Strother, J. A. & Paig-Tran, E. W. M. Manta rays feed using ricochet separation, a novel nonclogging filtration mechanism. *Sci. Adv.* **4**, eaat9533 (2018).
- Li, Z., Tan, C. M., Tio, W., Ang, J. & Sun, D. D. Manta ray gill inspired radially distributed nanofibrous membrane for efficient and continuous oil-water separation. *Environ. Sci.: Nano* **5**, 1466–1472 (2018).
- Schroeder, A., Marshall, L., Trease, B., Becker, A. & Sanderson, S. L. Development of helical, fish-inspired cross-step filter for collecting harmful algae. *Bioinspir. Biomim.* **14**, 056008 (2019).
- Aizenberg, J. et al. Skeleton of Euplectella sp.: structural hierarchy from the nanoscale to the macroscale. *Science* **309**, 275–278 (2005).
- Falcucci, G. et al. Adapting to the abyss: Passive ventilation in the deep-sea glass sponge Euplectella aspergillum. *Phys. Rev. Lett.* **132**, 208402 (2024).
- Fernandes, M. C., Aizenberg, J., Weaver, J. C. & Bertoldi, K. Mechanically robust lattices inspired by deep-sea glass sponges. *Nat. Mater.* **20**, 237–241 (2021).
- Falcucci, G. et al. Extreme flow simulations reveal skeletal adaptations of deep-sea sponges. *Nature* **595**, 537–541 (2021).
- Weaver, J. C. et al. Hierarchical assembly of the siliceous skeletal lattice of the hexactinellid sponge Euplectella aspergillum. *J. Struct. Biol.* **158**, 93–106 (2007).
- Zhou, X. et al. Recent advances in the modification of melamine sponge for oil-water separation. *J. Mater. Sci. Technol.* **207**, 209–224 (2025).
- Li, Z., Gao, T., Tian, K. & Wang, B. Elite-driven surrogate-assisted CMA-ES algorithm by improved lower confidence bound method. *Eng. Comput.* **39**, 2543–2563 (2023).
- Matsumoto, M. Vortex shedding of bluff bodies: a review. *J. Fluids Struct.* **13**, 791–811 (1999).
- Jalililab, Z., Amiri, A., Castagliola, P. & Khoo, M. B. C. Monitoring the coefficient of variation: A literature review. *Comput. Ind. Eng.* **161**, 107600 (2021).
- Fimbres-Weihs, G. A. & Wiley, D. E. Numerical study of mass transfer in three-dimensional spacer-filled narrow channels with steady flow. *J. Membr. Sci.* **306**, 228–243 (2007).
- Chiappini, D., Sbragaglia, M., Xue, X. & Falcucci, G. Hydrodynamic behavior of the pseudopotential lattice Boltzmann method for interfacial flows. *Phys. Rev. E* **99**, 053305 (2019).
- Falcucci, G. et al. Lattice Boltzmann models with mid-range interactions. *Commun. Comput. Phys.* **2**, 1071–1084 (2007).

28. Falcucci, G., Ubertini, S. & Succi, S. Lattice Boltzmann simulations of phase-separating flows at large density ratios: the case of doubly-attractive pseudo-potentials. *Soft Matter* **6**, 4357–4365 (2010).
29. Dollet, B., Scagliarini, A. & Sbragaglia, M. Two-dimensional plastic flow of foams and emulsions in a channel: experiments and lattice Boltzmann simulations. *J. Fluid Mech.* **766**, 28 (2015).
30. Fujiki, Y., Awai, H., Motoori, Y. & Goto, S. Attraction of neutrally buoyant deformable particles towards a vortex. *Phys. Rev. Fluids* **9**, 014301 (2024).
31. Höller, V., Radevik, K., Kiwi-Minsker, L. & Renken, A. Bubble columns staged with structured fibrous catalytic layers: residence time distribution and mass transfer. *Ind. Eng. Chem. Res.* **40**, 1575–1579 (2001).
32. Pangarkar, V. G., Yawalkar, A. A., Sharma, M. M. & Beenackers, A. A. C. M. Particle-liquid mass transfer coefficient in two-/three-phase stirred tank reactors. *Ind. Eng. Chem. Res.* **41**, 4141–4167 (2002).
33. Yu, Y., Pei, S., Zhang, J., Ren, N. & You, S. Bio-inspired porous composite electrode for enhanced mass transfer and electrochemical water purification by modifying local flow pattern. *Adv. Funct. Mater.* **33**, 2214725 (2023).
34. Landahl, M. T. & Mollo-Christensen, E. Turbulence and random processes in fluid mechanics. 2 edn. (Cambridge University Press 1992).
35. Mi, J., Jin, X. & Li, H. Cascade-Net for predicting cylinder wake at Reynolds numbers ranging from subcritical to supercritical regime. *Phys. Fluids* **35**, 075132 (2023).
36. Vincent Wong, K.-F., Barin, E. & Lane, J. Field experiments at the ohmsett facility for a newly designed boom system. *Spill Sci. Technol. Bull.* **7**, 223–228 (2002).
37. Wong, K.-F. V. & Barin, E. Oil spill containment by a flexible boom system. *Spill Sci. Technol. Bull.* **8**, 509–520 (2003).
38. Fang, J. & Wong, K.-F. V. Optimization of an oil boom arrangement. *Int. Oil Spill Conf. Proc.* **2001**, 1367–1374 (2001).
39. Lunde Hermansson, A. et al. Strong economic incentives of ship scrubbers promoting pollution. *Nat. Sustain.* 1-1 (2024).
40. Li, J. et al. Sustainable environmental remediation via biomimetic multifunctional lignocellulosic nano-framework. *Nat. Commun.* **13**, 4368 (2022).
41. Chen, Y. et al. Selective recovery of precious metals through photocatalysis. *Nat. Sustain.* **4**, 618–626 (2021).
42. Nie, Z., Lin, Y. & Tong, Q. Numerical simulations of two-phase flow in open-cell metal foams with application to aero-engine separators. *Int. J. Heat. Mass Transf.* **127**, 917–932 (2018).
43. Mazloomi M, A., Chikatamarla, S. S. & Karlin, I. V. Entropic Lattice Boltzmann Method for Multiphase Flows. *Phys. Rev. Lett.* **114**, 174502 (2015).
44. Bauer, M., Köstler, H. & Rüdte, U. lbmpy: Automatic code generation for efficient parallel lattice Boltzmann methods. *J. Comput. Sci.* **49**, 101269 (2021).
45. Dominik Schuster. Large scale simulations of swirling and particle-laden flows using the Lattice-Boltzmann Method. Fluid mechanics [physics.class-ph]. Institut National Polytechnique de Toulouse - INPT, English. (NNT: 2021INPT0063).(2021)
46. Hamann, L. & Blanke, A. Suspension feeders: diversity, principles of particle separation and biomimetic potential. *J. R. Soc. Interface* **19**, 20210741 (2022).
47. Taylor Michael, W., Radax, R., Steger, D. & Wagner, M. Sponge-associated microorganisms: evolution, ecology, and biotechnological potential. *Microbiol. Mol. Biol. Rev.* **71**, 295–347 (2007).

Acknowledgements

Project supported by the National Natural Science Foundation of China (Grant No. 52325003 [S.Y.], 52200190 [Y.Y.], 52070055 [J. Z.]), State Key Laboratory of Urban Water Resource and Environment (Harbin Institute of Technology, No. 2023DX03) [S.Y.], the China Postdoctoral Science Foundation (Grant No. 2022M720968) [Y.Y.] and the Heilongjiang Postdoctoral Foundation (Grant No. LBH-Z22143) [Y.Y.].

Author contributions

Y.Y.: Conceptualization, methods, software, formal analysis, investigation, writing - original draft, writing - review & editing, visualization, funding acquisition. C.D.: methods, software, formal analysis, investigation, data curation, writing - original draft, writing - review & editing, visualization. J.Z.: Investigation, validation, writing - original draft, writing - review & editing. N.R.: Methods, data curation, validation, supervision, writing - review & editing. C.Y.T.: Investigation, writing - original draft, writing - review & editing. S.Y.: Conceptualization, original draft, writing, focusing the investigation, methods, writing - review & editing, supervision, resources, funding acquisition.

Competing interests

The authors declare no competing interests.

Additional information

Supplementary information The online version contains supplementary material available at <https://doi.org/10.1038/s41467-024-55587-y>.

Correspondence and requests for materials should be addressed to Shijie You.

Peer review information *Nature Communications* thanks Wang Fenghe and the other, anonymous, reviewer(s) for their contribution to the peer review of this work. A peer review file is available.

Reprints and permissions information is available at <http://www.nature.com/reprints>

Publisher's note Springer Nature remains neutral with regard to jurisdictional claims in published maps and institutional affiliations.

Open Access This article is licensed under a Creative Commons Attribution-NonCommercial-NoDerivatives 4.0 International License, which permits any non-commercial use, sharing, distribution and reproduction in any medium or format, as long as you give appropriate credit to the original author(s) and the source, provide a link to the Creative Commons licence, and indicate if you modified the licensed material. You do not have permission under this licence to share adapted material derived from this article or parts of it. The images or other third party material in this article are included in the article's Creative Commons licence, unless indicated otherwise in a credit line to the material. If material is not included in the article's Creative Commons licence and your intended use is not permitted by statutory regulation or exceeds the permitted use, you will need to obtain permission directly from the copyright holder. To view a copy of this licence, visit <http://creativecommons.org/licenses/by-nc-nd/4.0/>.

© The Author(s) 2024